

A simple model for electron dissipation in trapped ion turbulence

M. Lesur, T. Cartier-Michaud, T. Drouot, P. H. Diamond, Y. Kosuga, T. Réveillé, E. Gravier, X. Garbet, S.-I. Itoh, and K. Itoh

Citation: *Phys. Plasmas* **24**, 012511 (2017); doi: 10.1063/1.4974269

View online: <http://dx.doi.org/10.1063/1.4974269>

View Table of Contents: <http://aip.scitation.org/toc/php/24/1>

Published by the [American Institute of Physics](#)



PFEIFFER VACUUM

**VACUUM SOLUTIONS
FROM A SINGLE SOURCE**

Pfeiffer Vacuum stands for innovative and custom vacuum solutions worldwide, technological perfection, competent advice and reliable service.

A simple model for electron dissipation in trapped ion turbulence

M. Lesur,^{1,2,a)} T. Cartier-Michaud,³ T. Drouot,¹ P. H. Diamond,⁴ Y. Kosuga,^{2,5} T. Réveillé,¹ E. Gravier,¹ X. Garbet,³ S.-I. Itoh,^{2,6} and K. Itoh^{6,7}

¹Institut Jean Lamour, Université de Lorraine, 54506 Vandoeuvre-lès-Nancy Cedex, France

²Research Institute for Applied Mechanics, Kyushu University, 816-8580 Kasuga, Japan

³CEA, IRFM, 13108 Saint-Paul-Léz-Durance Cedex, France

⁴CMTFO and CASS, University of California, San Diego, California 92093, USA

⁵Institute for Advanced Study, Kyushu University, 816-8580 Kasuga, Japan

⁶Research Center for Plasma Turbulence, Kyushu University, 816-8580 Kasuga, Japan

⁷National Institute for Fusion Science, 509-5292 Toki, Japan

(Received 16 September 2016; accepted 5 January 2017; published online 24 January 2017)

Trapped ion resonance-driven turbulence is investigated in the presence of electron dissipation in a simplified tokamak geometry. A reduced gyrokinetic bounce-averaged model for trapped ions is adopted. Electron dissipation is modeled by a simple phase-shift δ between density and electric potential perturbations. The linear eigenfunction features a peak at the resonant energy, which becomes stronger with increasing electron dissipation. Accurately resolving this narrow peak in numerical simulation of the initial-value problem yields a stringent lower bound on the number of grid points in the energy space. Further, the radial particle flux is investigated in the presence of electron dissipation, including kinetic effects. When the density gradient is higher than the temperature gradient, and the phase-shift is finite but moderate ($\delta \approx 0.02$), the particle flux peaks at an order-of-magnitude above the gyro-Bohm estimate. Slight particle pinch is observed for $\delta < 0.003$.
 Published by AIP Publishing. [<http://dx.doi.org/10.1063/1.4974269>]

I. INTRODUCTION

Experimental evidence points to drift-wave turbulence as the dominant source of cross-field transport of particles and energy in tokamaks. In this context, we aim at furthering the understanding of fundamental mechanisms involved in this complex, multiscale, coupled system.

A global effort has been ongoing, mainly in the last two decades, to develop the theory based on gyrokinetic numerical simulations.¹ The effort has been mainly focused on accuracy in real space, to include, e.g., realistic fusion experiment geometry, or modes with disparate scales, which are strongly modified by their coupling. On the other hand, the effort on accuracy in energy space is rather limited in the framework of drift-wave turbulence, although there is evidence of small-scale ($\Delta v_{\parallel} \ll v_{th}$) velocity-space structures in gyrokinetic simulation of drift-wave turbulence.² This poses a challenge for the conventional gyrokinetic approach, because resolving fine-scale structures in energy space makes such simulations very costly in terms of computing power.

There is a class of drift-waves that are driven by resonance with particle motion. In weakly collisional plasmas, resonant wave-particle interactions in general can lead to fine-scale structures in the velocity space. Therefore, we would like to propose a numerical investigation of resonance-driven drift-waves with a sufficient accuracy in the whole variable space. Here, “sufficient” remains to be quantified. To reach sufficient accuracy at reasonable cost, we sacrifice completeness for tractability.

In conventional gyrokinetics, the dynamics is described in a 4D phase-space parametrized by one adiabatic invariant. If we limit the kinetic description to magnetically trapped

particles, and rely on assumptions described in Section II, the bounce-averaged dynamics can be described in a reduced 2D phase-space, parametrized by the energy. The bounce-averaged gyrokinetic model for trapped ion precession resonance-driven turbulence^{3–7} is much more numerically tractable and allows a large increase in accuracy in velocity-space (thousands grid points in energy) at reasonable computing cost. As discussed in Section V, this makes it a promising toy model for bootstrapping the numerical investigation of drift-wave granulation. Recently, a semi-Lagrangian simulation code, TERESA, has been developed based on this model, making efficient use of parallel computing.^{8,9}

In the context of trapped ion resonance-driven turbulence, electron dissipation is an essential ingredient: it destabilizes a range of modes, often called as electron roots, which propagate in the electron diamagnetic direction,¹⁰ and it drives radial particle transport. Therefore, we apply in this paper an electron dissipation model to the reduced bounce-averaged gyrokinetic model. To be consistent with the idea of a minimum model, we model electron dissipation as a simple nonadiabatic modification of the Boltzmann response.^{10–13} It is expressed as a phase-shift between electron density and perturbed electric potential, $\hat{n}_e/n_0 = (1 + im\delta)e^{\hat{\phi}}/T_e$ (in Fourier space), where m is the mode number in precession angle, and δ is an input, constant parameter.

In Section III, we analyze the linear structure in energy space of the trapped ion resonance-driven mode. A strong peak is found at the resonant energy, with a narrow width at half maximum $\Delta E = 0.2 T_0$. This linear energy-space structure is stronger for higher electron dissipation. Resolving this peak with a 10% (1%) accuracy requires 256 (1024) grid points in the energy direction, which is significantly higher than the typical number of grid points in, e.g., parallel velocity in conventional gyrokinetic simulations.

^{a)}maxime.lesur@univ-lorraine.fr

Furthermore, kinetic effects may play an important role in radial transport. In Section IV, we investigate the peak radial particle flux. The dependency of peak particle flux on δ is similar to that of the maximum linear growth rate. When the density gradient and temperature gradient are similar, particle flux is of the order of a gyro-Bohm estimate for high enough electron dissipation, $\delta > 0.005$. When the density gradient is significantly larger than the temperature gradient, that is, when there are electron roots with growth-rates comparable to that of most unstable ion roots, particle flux peaks at an order-of-magnitude above the gyro-Bohm estimate for $\delta > 0.005$. Slight, transient particle pinch is observed in the case of higher density gradient, for smaller values of δ .

II. MODEL

We adopt a reduced bounce-averaged gyrokinetic model, which was developed by Depret,⁵ Sarazin,⁶ and Darmet,⁷ based on the Tagger-Pellat-Diamond-Biglari model.^{3,4} The bounce-averaged gyrokinetic distribution f of trapped ions (or “banana centers”) satisfies a kinetic equation

$$\frac{\partial f}{\partial t} + [J_0 \phi, f]_{\alpha, \psi} + E \Omega_d \frac{\partial f}{\partial \alpha} = 0. \quad (1)$$

Here, $E \Omega_d = \omega_d$ is the energy-dependent precession frequency, and $[\dots]_{\alpha, \psi}$ are Poisson brackets in the phase-space of toroidal precession angle α and poloidal magnetic flux ψ (which plays the role of radial coordinate). Furthermore, J_0 is an operator that performs two successive averages: a gyro-average (on a cyclotron motion) and a bounce-average (on a banana orbit). Here, physical quantities are normalized as listed in Table I.

This reduced model relies on the following assumptions:

- The equilibrium configuration is that of a large aspect ratio tokamak. However, the inverse aspect ratio ϵ must not be so small that the fraction $f_p \sim \sqrt{\epsilon}$ of trapped particles is negligible.
- Resonant interactions are dominated by strongly trapped ions. In this case, we can neglect the radial variation of precession frequency, and we focus on a single value of the pitch-angle.
- The mode frequency is much lower than the passing ion transit frequency.

TABLE I. Normalization. Physical quantities are noted without a hat, and dimensionless quantities with a hat. Here, $\omega_{d,0} \equiv q_0 T_0 / (e r_0 R_0 B_0)$ is a typical precession frequency of strongly trapped ions at $E = T_0$, n_0 and T_0 are arbitrary normalizing ion density and temperature such that $\hat{n} = \hat{T} = 1$ at $\hat{\psi} = 1$, and L_ψ is the radial size of the simulation box in magnetic flux units. Note that the minor radius a , the Larmor radius ρ_0 , and the banana width δ_b are all expressed in units of Ψ here. In the main text, the notation “” is omitted for clarity.

Quantity	e.g.	Normalization
Time	t, ω^{-1}	$\hat{t} = \omega_{d,0} t$
Length	r	$\hat{r} = r (B_0 / q_0 L_\psi)^{1/2}$
Poloidal magnetic flux	$\psi, a, \rho_0, \delta_b$	$\hat{\psi} = \psi / L_\psi$
Electric potential perturbation	ϕ	$\hat{\phi} = \phi / (\omega_{d,0} L_\psi)$
Energy	E	$\hat{E} = E / T_0$
Density	n	$\hat{n} = n / n_0$
Temperature	T	$\hat{T} = T / T_0$

- The plasma is at low- β , for which trapped ion precession resonance-driven modes are mostly electrostatic.

Self-consistency is ensured by a quasi-neutrality constraint, including a polarization term $\bar{\Delta} \phi$, which involves a non-isotropic Laplacian operator

$$\bar{\Delta} \equiv \left(\frac{q_0 \rho_0}{a} \right)^2 \frac{\partial^2}{\partial \alpha^2} + \delta_b^2 \frac{\partial^2}{\partial \psi^2}. \quad (2)$$

Here, ρ_0 is the ion Larmor radius, and δ_b is the trapped-ion banana width.

Conventionally, an adiabatic response of electrons is assumed. Here, we take into account the non-adiabatic response of electrons, due to collisional dissipation. In the literature, several ways have been adopted to model electron dissipation:

- (1) solving a kinetic equation for trapped electrons as well and including a collision operator,
- (2) constant phase-shift implemented by a term of the form $i\delta$ in the Poisson equation,
- (3) an *ad hoc* model with an arbitrary cut-off for high mode numbers.¹⁴

Here, we adopt the approach number 2. We write the Poisson equation as

$$\begin{aligned} C_1 \left[\phi - \langle \phi \rangle + \mathcal{F}^{-1} \left(i \delta_m \hat{\phi}_m \right) \right] - C_2 \bar{\Delta} \phi \\ = \frac{2}{\sqrt{\pi}} \int_0^\infty J_0(E) f \sqrt{E} dE, \end{aligned} \quad (3)$$

where \mathcal{F}^{-1} is the inverse Fourier transform operator, and $\hat{\phi}_m$ is the m -th component of the Fourier decomposition in α of ϕ . Here, $C_1 = \tau C_2 / f_p$ and $C_2 = e \omega_{d,0} L_\psi / T_0$ are dimensionless, constant input parameters, which account for the fraction of trapped particles f_p and ion/electron temperature ratio τ . The average $\langle \phi \rangle$ is an average on the angle α . Electron dissipation is modeled by a phase-shift between ϕ and density perturbation, $\delta_m \equiv m\delta$, where δ is a constant, real, input parameter. This approximation stems from the linearized drift-kinetic equation for electrons. Here, we have assumed $\nu_{e,i} / \epsilon_0 < \omega \sim \omega_* < \nu_{i,i} / \epsilon_0$, where ω_* is a diamagnetic drift frequency, and $\nu_{e,i}$ and $\nu_{i,i}$ are ion-electron and ion-ion collision frequencies. In this regime, δ can be approximated as $\delta \approx \epsilon_0^{3/2} \omega_* \eta_e / \nu_{ei}$, where $\eta_e = d \ln T_e / d \ln n_e$ is the ratio between gradients in equilibrium electron density and temperature profiles.

The advantages of method 2 are (a) decreased computation cost, (b) analytical tractability, and (c) consistency with the idea of a minimalist kinetic model with necessary ingredients only. An analogy can be made between the phase-shift δ in trapped-ion turbulence and the wave dissipation rate γ_d in the Berk-Breizman model for the bump-on-tail instability.¹⁵ Both are minimalist models for investigating fundamental physical mechanisms introduced by dissipation in resonance-driven instabilities.

We have implemented the $i\delta_m$ term in the TERESA code. As a first verification, we confirm in Appendix A the expected relationship between density and potential perturbations during the linear phase for unstable modes. As further verification, the simulations are compared with solutions of the dispersion relation in Appendix B. Note that in

Appendix C, we derive an analytic, explicit expression for the linear frequency and growth rate of the ion root ($\text{Re}(\omega) > 0$), including the dissipation term, in the limit of small growth rate $\gamma/\omega \ll 1$.

In this paper, the TERESA simulations are performed with thermal baths at both inside boundary $\psi = 0$ and outside boundary $\psi = 1$. Artificial dissipation is imposed in buffer regions $\psi < 0.15$ and $\psi > 0.85$ to smooth out the transition between turbulent fluctuations ϕ , and the constraint $\phi = 0$ at $\psi = 0$ and $\psi = 1$.

Throughout this paper, the equilibrium distribution function is chosen as

$$F_{\text{eq}}(\psi, E) = e^{-E} [1 + (\kappa_T(E - 3/2) + \kappa_n)(1 - \psi)], \quad (4)$$

where $\kappa_n \equiv -\partial \log n_{\text{eq}} / \partial \psi|_{\psi=1}$ measures the equilibrium density gradient, and κ_T measures the temperature gradient, similarly. This is a first-order Taylor expansion of $n_{\text{eq}} T_{\text{eq}}^{-3/2} \exp(-E/T_{\text{eq}})$ at $\psi = 1$, which was also adopted in Refs. 5, 16, and 17 (but with a different definition of ψ , where $\psi = 1$ at the core, $\psi = 0$ at the edge).

III. ENERGY-SPACE STRUCTURE

Let us consider a flat density profile, $\kappa_n = 0$. The input parameters of the model are shown as *Case 1* in Table II. In this case, the dispersion relation yields a branch with positive real frequency, which corresponds to propagation in the ion diamagnetic direction. It is often called as the ion root.

We investigate the linear energy-space structure of the ion root of the trapped-ion-mode. This eigenfunction is obtained from single-mode TERESA simulations by extracting at a fixed time t_1 a single m Fourier component of $f(x, \psi_{1/2}, E, t_1)$, where $\psi_{1/2} = 0.5$ corresponds to the mid-radius of the simulation box. It is then normalized by the absolute value of the m component of $\phi(x, \psi_{1/2}, t_1)$. The time of snapshot t_1 is chosen around the end of the exponential growth (and before the decrease of growth-rate due to nonlinear saturation), in order to give enough time for the eigenfunction to form from the initial arbitrary perturbation. In this section, the hat notation for Fourier components is omitted.

Fig. 1 shows the eigenfunction δf_m , for an arbitrary mode number, $m = 10$, obtained from a simulation with $N_E = 2048$ grid points in energy. We compare two cases, without ($\delta = 0$, left) and with ($\delta = 0.02$, right) electron dissipation. In both cases, there is a peak at $E/T_0 \approx \omega/(m\Omega_d)$, which corresponds to the resonance $\omega = m\omega_d(E)$. Interestingly, this peak becomes stronger as δ increases.

Note that the peak is narrow, especially for the imaginary part, with a full width at half maximum $\Delta E = 0.2 T_0$ in the case of Fig. 1(b). We have performed a scan (restricted to powers of 2) in the number N_E of grid points in the energy direction. We found that obtaining the eigenfunction within a 10% accuracy requires $N_E = 256$ grid points (here, the energy

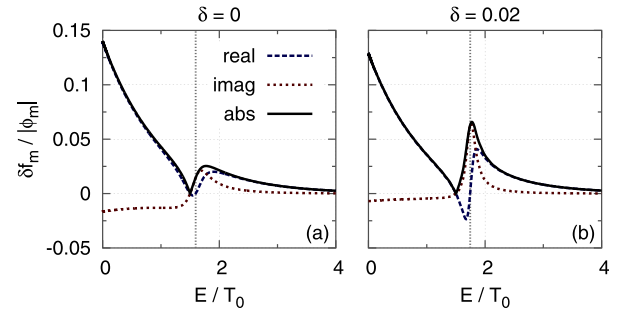


FIG. 1. Eigenfunction for Case 1 (flat density profile), $m = 10$, at $\psi = 0.5$. (a) No electron dissipation. (b) Finite electron dissipation $\delta = 0.02$. A dotted vertical line corresponds to the energy such that the resonance condition $\omega = m\omega_d(E) = m\Omega_d E$ is satisfied.

cut-off is $E_{\text{max}} = 20 T_0$). A 1% accuracy requires $N_E = 1024$ grid points. That is true even though we adopted a regular grid spacing in \sqrt{E} (rather than in E), which favors the resolving of small-scale structures at relatively low energies $E \sim T_0$.

We investigated the impact of sub-resolution of the resonance in the energy space on the linear growth rate, and the peak field amplitude (of mode $m = 10$ only). Table III gives the relative errors for $N_E = 24, 48, 96, 192$, and 384, taking a simulation with $N_E = 1536$ as a reference case. Here, the structure of the grid in energy is homogeneous in $E^{1/2}$. We have also performed simulations with different grid structures, namely, homogeneous in E , or homogeneous in $E^{1/3}$, but these lead to slightly increased inaccuracies.

In the limit of small ρ_0 and δ_b , the eigenfunction can be estimated as

$$\delta f_m = -\frac{m\kappa_T e^{-E}(E - 3/2)}{\omega - m\Omega_d E + i\gamma} \phi_m. \quad (5)$$

With the simple approximation $\phi_m = |\phi_m|$, the latter expression is in quantitative agreement with the values from numerical simulation (Fig. 1). The maximum absolute error in terms of $|\delta f_m|/|\phi_m|$ is 0.0016 for $\delta = 0$ and 0.0069 for $\delta = 0.02$. Eq. (5) does not depend explicitly on δ . In fact, here, the dominant cause of shrinking of the resonance with finite electron dissipation is a twice smaller γ/ω ratio for $\delta = 0.02$ compared to $\delta = 0$.

IV. NONLINEAR ANALYSIS

Let us consider a typical time evolution of an initial value TERESA simulation. After a linear phase, the electric field energy first saturates to some peak value, before decaying to a quasi-steady-state average value. We focus on the first, transient peaking of electric field amplitude, which corresponds also to the highest peak of both field amplitude and particle flux. Understanding the first and strongest peak may serve the understanding of the quasi-steady state.

TABLE II. Input parameters.

	C_1	C_2	Ω_d	$q_0 \rho_0 / a$	δ_b	κ_T	κ_n
Case 1	0.1	0.1	1	0.01	0.1	0.15	0
Case 2	0.1	0.1	1	0.01	0.1	0.1	0.2
Case 3	0.1	0.1	1	0.01	0.1	0.15	0.15

TABLE III. Impact of sub-resolution in energy space. Relative error (in percent), taking a $N_E = 1536$ simulation as the reference case.

N_E	24	48	96	192	384
Linear growth rate	63	4.6	2.6	0.013	3.6×10^{-6}
Peak field amplitude	50	1.3	2.2	0.063	5.8×10^{-4}

We ran a series of TERESA simulations for the three cases of Table II and various values of electron dissipation rate δ . For these simulations, we use $N_\psi = 257$ grid points in radius, $N_\alpha = 513$ grid points in precession angle, and $N_E = 1024$ grid points in energy, with an energy cut-off $E_{\max} = 20$. This fine grid in energy is necessary to obtain the flux with good accuracy, at least in some cases. Indeed, similar to the former section on the energy-space structure, although simulations with coarser grids ($N_E = 96 - 256$) suffice to obtain a qualitative trend, a statistical quantitative convergence requires finer grids ($N_E = 512 - 1024$). Fig. 2 shows the peak field energy (a), peak zonal flow energy (b), and peaks (minimum and maximum) of radial particle flux at $\psi = 0.5$ (c). Here, the field energy is defined as $e\tilde{\phi}/T$, where $\tilde{\phi}$ is the root mean square (rms) of $\phi - \langle \phi \rangle_\alpha$, over a radial domain $0.25 < \psi < 0.75$, which excludes the buffer regions. The zonal flow energy is defined as $e\phi_0/T$, where ϕ_0 is the rms of ϕ , over the same radial domain. The radial particle flux Γ_ψ is defined such that the angle-averaged density satisfies $\partial \langle n \rangle_\alpha / \partial t + \partial \Gamma_\psi / \partial \psi = 0$ in the absence of source.

Unsurprisingly, the dependency of peak particle flux on δ is similar to that of the maximum linear growth rate (see Fig. 7(b) for a graph of γ against δ). However, peak field and

zonal energies show a different behavior, especially in the presence of a density gradient, peaking at $\delta \approx 0.005$ even though γ peaks at $\delta \approx 0.02$. In the case of the flat density profile (Case 1), field energy, zonal energy, and particle flux all decrease roughly monotonously with δ .

Let us compare the particle flux in Case 2 and Case 3, in the presence of finite dissipation, $\delta > 0.005$, after normalizing it by a gyro-Bohm estimate $\Gamma_{gB} = \rho^* T_0 / (eB_0) \partial n / \partial r$. If we choose $q_0 \epsilon / \rho^* = 40$, the flux peaks at $\Gamma_\psi / \Gamma_{gB} \approx 8$ for Case 2, and $\Gamma_\psi / \Gamma_{gB} \approx 1$ for Case 3. We note that from linear analysis, it can be concluded that electron roots have larger growth rates in Case 2 than in Case 3 for fixed δ . Therefore, electron roots may be responsible for pushing the particle flux up to an order-of-magnitude above the gyro-Bohm estimate.

Interestingly, when density gradient dominates (Case 2), we observe a slight pinch of particle ($\Gamma_\psi < 0$) for $\delta \approx 0.0015 - 0.002$, where the most unstable mode propagates in the electron diamagnetic direction. This can be seen in the inset of Fig. 2(c). The pinch can also be seen in Fig. 3, which shows a spatio-temporal map of the particle flux for Case 2 and $\delta = 0.0015$. The pinch is strongest at time $t \approx 3.3$ and stays significant in later times around the mid-radius of the simulation box ($\psi \approx 0.5$). To invoke a density pinch, we need to check that the negative flux is not due to a reversed density gradient. Between $t = 3.0$ and $t = 3.7$ (time period during which the negative flux is most significant), the density gradient is never reversed throughout all the simulation box. More precisely, the gradient $-\partial n / \partial \Psi$ stays larger than $0.1n_0 / L_\Psi$ (about half of the initial κ_n) if we exclude the buffer regions and larger than $0.078n_0 / L_\Psi$ if we include them. When density gradient and temperature gradient are similar (Case 3), we observe a weaker pinch at $\delta = 0.002$.

As a caveat, the model adopted in this paper does not allow to accurately characterize the nonlinear saturation. Indeed, it was shown that saturation is achieved via a spectral transfer that involves electron drift waves.^{18,19} Investigating the quasi-steady-state obtained in our simulations may be relevant, for example, to reveal hints of new physical mechanisms, but not for quantitative interpretation or prediction of experimental data.

V. APPLICATIONS

The bounce-averaged gyrokinetic model is not to be readily applied to the quantitative interpretation or prediction of complex experimental devices such as toroidal fusion experiments, which couple the electromagnetic dynamics of both trapped and passing particles, both ions and electrons, including supra-thermal (energetic) particles. However, it shows that one can perform numerical analysis of resonance-driven drift-wave turbulence, as an isolated building block of a complex system of coupled blocks (for the purpose of improved understanding), with a great accuracy in all variables (including energy), at reasonable computing cost.

Furthermore, the present work provides some basis on the way to numerical investigation of nonlinear phenomena that involve strong wave-particle resonances and require a high accuracy in velocity-space. More than four decades ago, Dupree proposed a novel turbulent state, characterized by the presence, not only of a collection of waves with

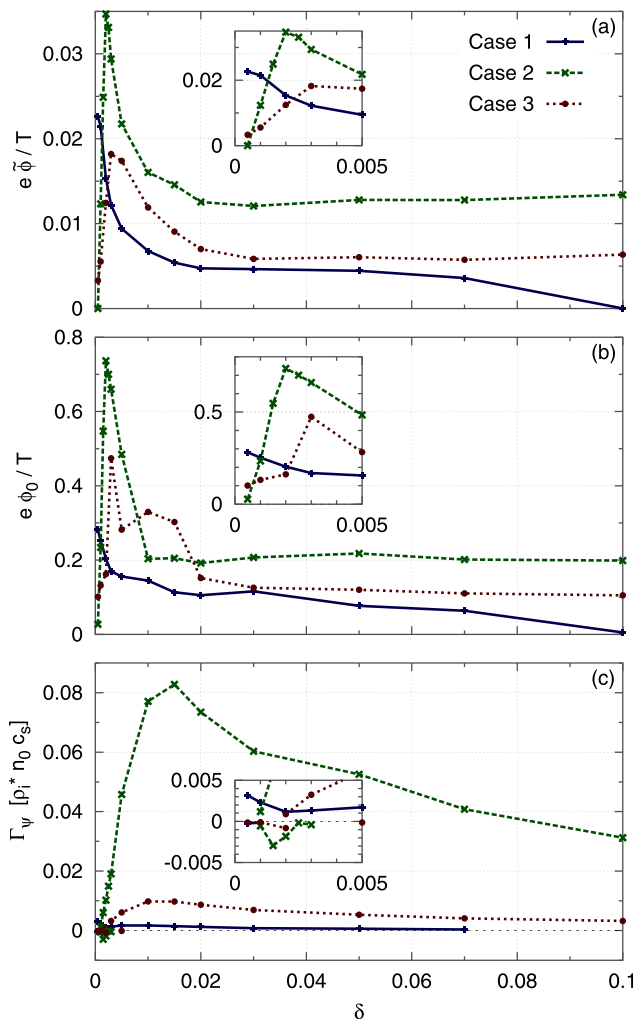


FIG. 2. Peak field energy (a), peak zonal flow energy (b), and peaks (minimum and maximum) of radial particle flux (c), as a function of electron dissipation. Inset: zoom in the low δ region. For clarity, the particle flux is plotted when $|\Gamma_\psi| < 10^{-4}$.

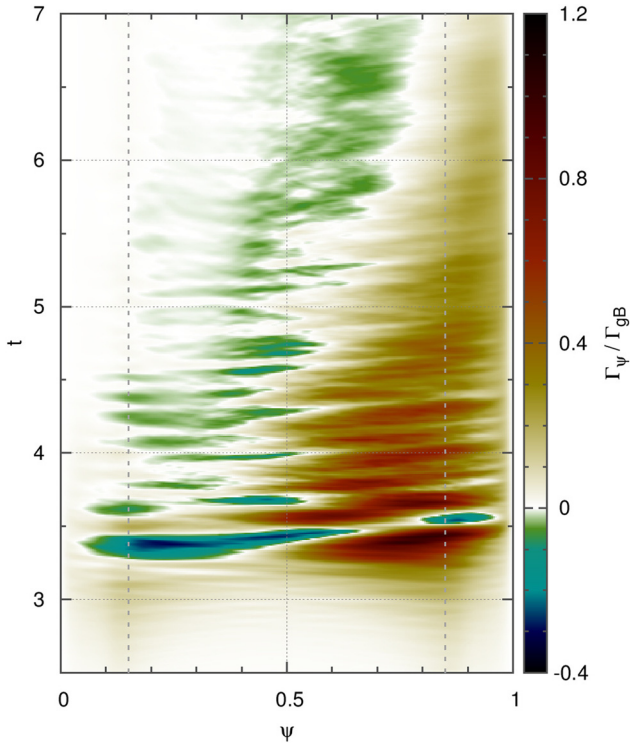


FIG. 3. Radial particle flux, as a function of radius and time, for Case 2 and $\delta = 0.0015$. Here, the flux is normalized by a gyro-Bohm estimate $\Gamma_{gB} = \rho^* T_0 / (eB_0) \partial n / \partial r$, with $q_0 \epsilon / \rho^* = 40$. Dashed vertical lines indicate the boundary with buffer regions, near the magnetic axis $\psi = 0$ and the outer region $\psi = 1$, where artificial dissipation dominates.

random phases, but also of small-scale structures in the phase-space of particle distribution.²⁰ In a limit of narrow wave spectrum, these structures would take the form of Bernstein-Green-Kruskal (BGK) modes,²¹ with a vortex structure in phase-space. For a wide wave spectrum, though, which is more relevant to drift-wave turbulence, there is a competition between the formation by wave-particle resonance of BGK modes, and their dispersion by the ambient turbulence. The result of this competition is predicted, by the analytic theory, to take the form of a smaller scale (compared to BGK modes) random granulation of phase-space.

More recently, many authors have discussed the importance of granulation in drift-wave turbulence and transport,^{3,22–27} based on various analytic models. Numerical investigation remains to be performed. This poses a challenge for the conventional gyrokinetic approach, because resolving fine-scale structures in energy space makes such simulation very costly in terms of computing power. Attempts have been made to resolve fine-scale velocity-space structures in local gyrokinetic simulation.² Evidence of small-scale ($\Delta v_{\parallel} \ll v_{th}$) structures was found, but the link to granulation was not discussed.

In the context of granulation, electron dissipation is an essential ingredient: it drives the nonlinear growth of phase-space structures,³ introduces dynamical friction associated with anomalous transport of ion heat and particles due to ion phase-space structures,³ and yields an important contribution to Reynolds stress, which can drive toroidal flows.²⁸ The trapped-ion reduced model with simple $i\delta$ electron dissipation is a promising tool to bootstrap the numerical study of granulation in drift-wave turbulence.

However, one must keep in mind the limitations of this simple electron dissipation model. As was pointed out by Crotinger and Dupree, the $i\delta$ approximation misses the effect of spectral broadening in regimes of strong turbulence and does not give the correct response to a coherent structure.¹⁴ Therefore, in the long term, numerical studies of granulation will require more advanced models.

VI. CONCLUSION

The linear eigenfunction of the resonance-driven trapped ion mode features a peak at the resonant energy, which is stronger for finite electron dissipation compared to no electron dissipation. In the case of finite electron dissipation, with a phase-shift $\delta_m = 0.02m$ between the m toroidal component of electron density and electric potential perturbations, the peak is narrow, $\Delta E = 0.2 T_0$. It requires a large number of grid points in energy space to be resolved accurately.

Kinetic numerical simulations of trapped-ion dynamics were applied to investigate the peak radial particle flux. Particle flux depends strongly on the ordering between equilibrium density gradient κ_n and equilibrium temperature gradient κ_T . The particle flux was compared to a gyro-Bohm estimate, Γ_{gB} . Particle flux peaks to $\sim \Gamma_{gB}$ and $\approx 8\Gamma_{gB}$, for $\kappa_n \approx \kappa_T$ and $\kappa_n \approx 2\kappa_T$, respectively, and for large-enough electron dissipation. Furthermore, it can take negative values, $\approx -0.4\Gamma_{gB}$, for small but finite electron dissipation $\delta_m \approx 0.005m$.

Recently, a promising mean of control of heat transport was found in the framework of TERESA.²⁹ In addition, the nonlinear dynamics in TERESA was found to involve strong and fast interactions between streamers and zonal flows.^{30,31} In future works, we will investigate whether electron dissipation impacts the former heat transport and the latter interactions. Finally, we will focus on the steady-state in flux-driven simulations, and the presence of granulation, based on the present model and numerical code. Therefore, this paper also serves as a basis for future studies.

ACKNOWLEDGMENTS

This work was supported by the French Research Federation for Magnetic Fusion Studies, by the JSPS, Japan (16K18335, 16H02442, 15K18305, 15H02155, 23244113, and 15H02335), by the collaboration programs of the RIAM of Kyushu University and of NIFS (NIFS14KNST072, NIFS15KNST089), and Asada Science Foundation.

APPENDIX A: PHASE-SHIFT

In this Appendix, we analyze the impact of electron dissipation on the relation between potential perturbations and density perturbations in TERESA^{8,9} simulations. We transform the potential and density perturbations to Fourier space in precession angle, $\hat{\phi}_m$ and $\hat{\delta}n_m$. Fig. 4 shows the amplitude ratios $|\hat{\delta}n_m|/|\hat{\phi}_m|$ and the phase shifts $\arg(\hat{\delta}n_m/\hat{\phi}_m)$, for a time $t=1.0$ during the linear growth. Here, we choose $\delta = 0.01$. As expected, for the most unstable modes ($m = 5 - 20$), the amplitude ratios are nearly constant with respect to m (and t), and the phase-shifts scale as $m\delta$.

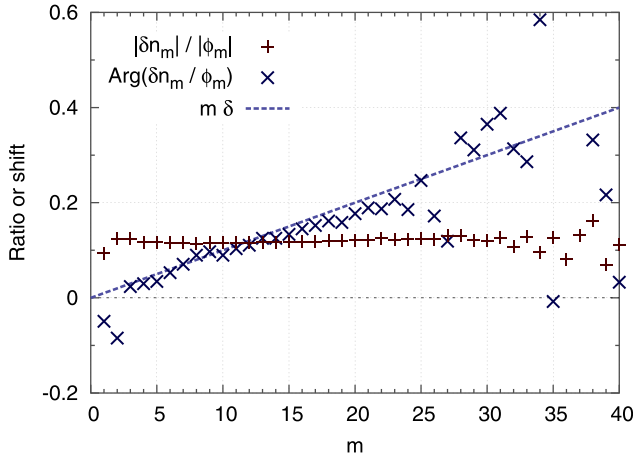


FIG. 4. Amplitude ratios and phase-shifts as a function of the toroidal mode number m , for Case 1, with $\delta = 0.01$, at $t = 1$.

Later, during the nonlinear saturation, the amplitude ratios and phase-shifts become apparently random.

APPENDIX B: LINEAR ANALYSIS

In this Appendix, we analyze the frequency and growth rate of both ion and electron roots in the presence of electron dissipation. We can summarize the results as follows. In the limit of zero equilibrium density gradient, the growth rate decreases monotonously with δ . On the other hand, it peaks at $\delta \approx 0.02$ when the density gradient is comparable to the temperature gradient. When the density gradient exceeds the temperature gradient, the most unstable mode propagates in the electron diamagnetic direction for $\delta < 0.02$. The results are in qualitative agreement with analytic theories of trapped-ion modes in the literature.^{4,10}

1. Dispersion relation

Linearizing Eqs. (1)–(3), we obtain the dispersion relation $D(x) = 0$, where $x = \omega/(m\Omega_d)$, and

$$D(x) = C_r + iC_1\delta_m + \frac{2}{\sqrt{\pi}} \int \frac{\sqrt{E}}{E-x} \frac{\partial F_{eq}}{\partial \psi} J_0^2(E) dE. \quad (\text{B1})$$

In the latter expression, the integral is on a Landau path, and

$$C_r = C_1 + C_2(m^2 q_0^2 \rho_0^2 / a^2 + k^2 \delta_b^2). \quad (\text{B2})$$

In the $\delta \rightarrow 0$ limit, Eq. (B1) is in agreement with Ref. 5. In this case, the marginal solution is $\omega = \omega_0$, where $\omega_0 \equiv 3m\Omega_d/2$.

Substituting the equilibrium distribution function, Eq. (4), yields

$$D(x) = C_r + iC_1\delta_m - \kappa_T I_r - \frac{2}{\sqrt{\pi}} \left[\kappa_n + \kappa_T \left(x - \frac{3}{2} \right) \right] \int \frac{\sqrt{E} e^{-E}}{E-x} J_0^2(E) dE, \quad (\text{B3})$$

where

$$I_r = \frac{2}{\sqrt{\pi}} \int_0^\infty \sqrt{E} e^{-E} J_0^2(E) dE. \quad (\text{B4})$$

In the limit of small density gradient ($\kappa_n \rightarrow 0$), the latter dispersion relation yields a branch with positive real frequency, which corresponds to propagation in the ion diamagnetic direction. It is often called as the ion root. In the opposite limit of small temperature gradient ($\kappa_T \rightarrow 0$), the latter dispersion relation yields a root with negative real frequency, which corresponds to propagation in the electron diamagnetic direction. However, it cannot be unstable unless electron dissipation is finite $\delta > 0$. It is often called as the dissipative electron root. This is consistent with previous works.¹⁰ In the reminder of this Appendix, we analyse the impact of electron dissipation on linear frequency and growth rate in various regimes.

2. Ion root

Let us consider a flat density profile, $\kappa_n = 0$, and explore the ion root of the trapped-ion-mode. The input parameters of the model are shown as *Case 1* in Table II.

The result from TERESA simulations, as well as the numerical solution of dispersion relation Eq. (B3), is shown in Fig. 5 against the electron dissipation rate δ . Furthermore, in Appendix C, we solve the dispersion relation Eq. (B3) for the ion root, perturbatively, up to the second order in $(\omega - \omega_0)$. The solution is included in Fig. 5. We observe a quantitative agreement between analytic and numerical solution of the dispersion relation, as well as with the numerical simulation, for both the real frequency and the growth rate. The goal of Fig. 5 is only to provide a test for (1) our implementation of electron dissipation in TERESA, (2) our numerical dispersion relation solver, and (3) our analytic theory.

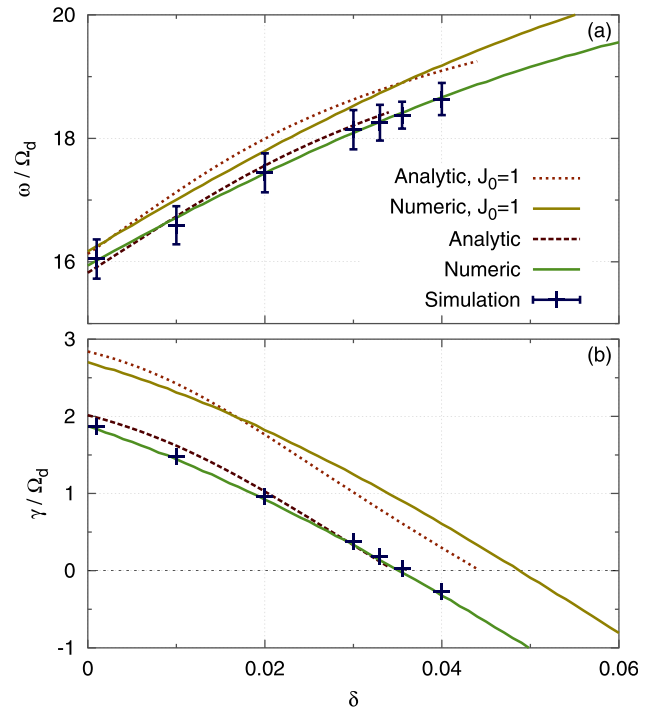


FIG. 5. Linear frequency (a) and growth rate (b) as a function of electron dissipation, for Case 1 (flat density profile), for a given mode. The mode numbers are arbitrarily chosen as $m = 10$ and $k = \pi$. The legend is shared between (a) and (b). “Analytic,” “Numeric,” and “Simulation” refer to Eq. (C14), numerical solution of Eq. (B3), and TERESA initial value simulation, respectively.

Hereafter, let us apply the numerical solver of dispersion relation Eq. (B3), alone, to explore the impact of electron dissipation on the various instabilities.

Fig. 6 shows the frequency (a) and linear growth rate (b) of modes with different wavelengths. Most strikingly, electron dissipation significantly mitigates the global instability for values $\delta \sim 0.01$ (although the $m = 1$ mode is not stabilized unless $\delta > 0.37$). In addition, increasing electron dissipation significantly decreases the wavelength of the most unstable mode. The impact of dissipation (for reasonable values $\delta \ll 1$) on the real frequency is negligible, for each mode taken separately.

We include in Fig. 6 the linear solution for $k = 2\pi$, to illustrate the fact that modes with radial mode numbers $k/\pi > 1$ are much more stable than modes with $k = \pi$. We also include the analytic expression Eq. (C14) to demonstrate that it is valid for many mode numbers.

Fig. 7 (case 1) summarizes the impact of electron dissipation on the most unstable mode. From this point of view, the real frequency (of the most unstable mode) significantly decreases with electron dissipation, even though the frequency for a given m slightly increases. The reason is that the mode number of the most unstable mode significantly decreases with increasing electron dissipation. The propagation stays in the ion diamagnetic direction ($\omega > 0$). The growth rate decreases monotonically as dissipation increases. The impact of dissipation on all frequency, growth rate, and mode number is almost linear for $\delta < 0.01$. The growth rate in the adiabatic electron limit ($\delta = 0$) is $\gamma \approx 3\omega_d$.

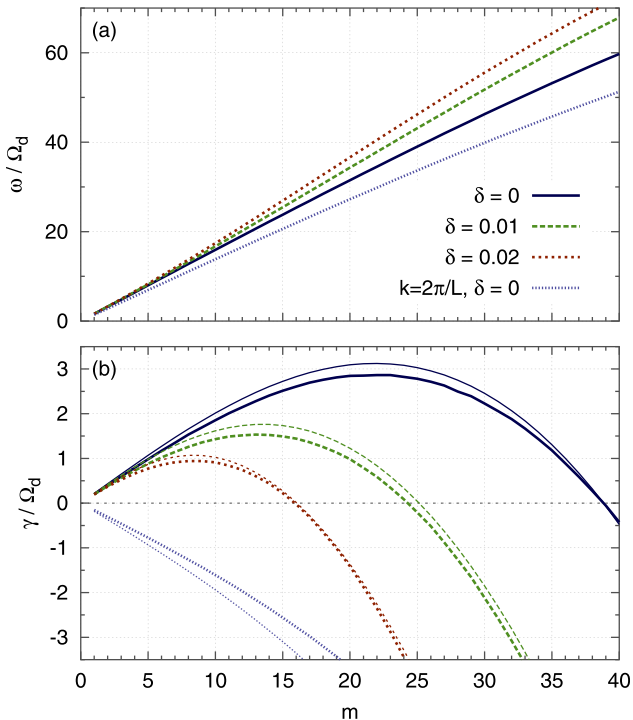


FIG. 6. Linear frequency (a) and growth rate (b) as a function of the toroidal mode number, for Case 1 (flat density profile). The radial mode number is $k = \pi$ except for one curve for $k = 2\pi$. The legend is shared between (a) and (b). Thin curves correspond to the analytic expression Eq. (C14).

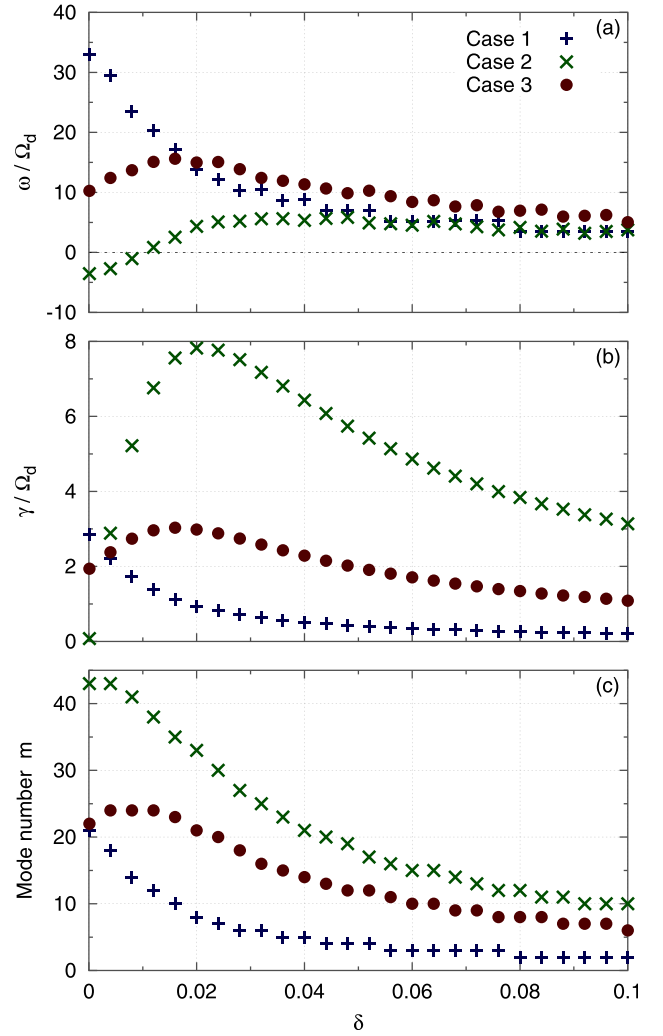


FIG. 7. Linear frequency (a), growth rate (b), and mode number (c) of the most unstable mode, as a function of electron dissipation.

3. Electron root

Let us consider a case where the equilibrium density gradient is larger than the temperature gradient and explore the electron root of the trapped-ion-mode. The input parameters of the model are shown as *Case 2* in Table II.

The numerical solution of dispersion relation Eq. (B3) is shown in Fig. 7 against electron dissipation rate δ . In this regime, the growth rate is zero for $\delta = 0$, but positive for finite δ . It peaks to $\gamma \approx 8\omega_d$ at $\delta \approx 0.02$. For $\delta < 0.01$, the most unstable mode, which has a relatively high mode number $m > 40$, propagates in the electron diamagnetic direction ($\omega < 0$), and growth rate is an increasing function of δ . On the contrary, for $\delta > 0.02$, the most unstable mode propagates in the ion diamagnetic direction, and growth rate is a decreasing function of δ , which appears to saturate to a finite value for large δ .

Fig. 8 shows in more detail how the frequency and growth rate depend on δ , for finite but small δ , not only for the most unstable mode but also for a large range of mode numbers. We observe that, even when the most unstable mode is an ion root, there can be unstable electron roots as well with comparable growth rates and lower mode numbers

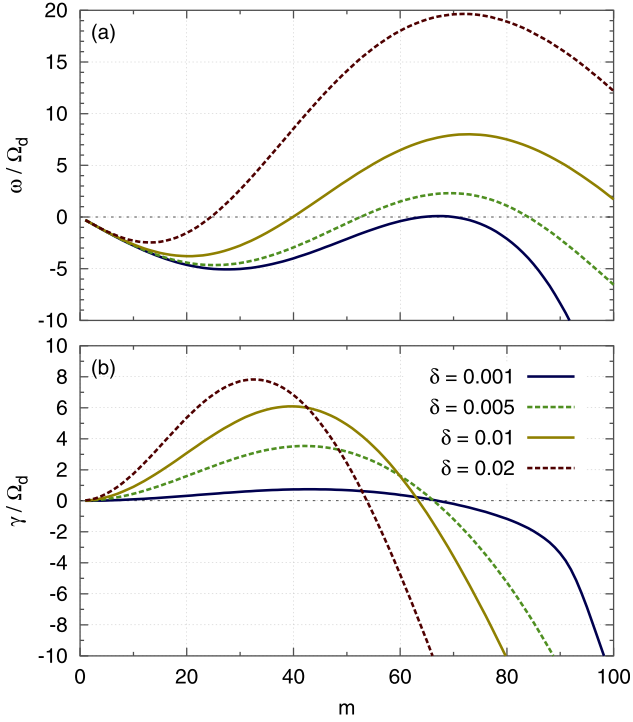


FIG. 8. Linear frequency (a) and growth rate (b) as a function of the toroidal mode number, for Case 2 (higher density gradient). The radial mode number is $k = \pi$.

(e.g., for $\delta = 0.005$). Conversely, dominant electron roots can coexist with ion roots with comparable growth rates (e.g., for $\delta = 0.02$).

4. Competition between ion and electron roots

Let us consider equilibrium profiles with comparable gradients to study the competition between ion and electron roots of the trapped-ion-mode. We choose $\kappa_n = \kappa_T = 0.15$. The input parameters of the model are shown as *Case 3* in Table II.

The numerical solution of dispersion relation Eq. (B3) is shown in Fig. 7 against electron dissipation rate δ . In this regime, the growth rate is finite ($\gamma \approx 2\omega_d \approx 0.2\omega$) for $\delta = 0$. It peaks to $\gamma \approx 3\omega_d$ at $\delta \approx 0.02$. Propagation is in the ion diamagnetic direction. Dependence of the growth rate on electron dissipation is relatively weak.

APPENDIX C: ANALYTIC EXPRESSION OF LINEAR FREQUENCY AND GROWTH RATE

In this Appendix, we derive an analytic, explicit expression for the linear frequency and growth rate of the ion root ($\text{Re}(\omega) > 0$), from the dispersion relation Eq. (B3), in the limit of small growth rate $\gamma/\omega \ll 1$.

As a first step for the sake of clarity, we approximate the gyroaveraging operator by $J_0 = 1$. This is valid in the limit of small banana width $\delta_b \ll 1$ (and small gyroradius). With $J_0 = 1$, $I_r = 1$ and the dispersion relation become

$$D(x) = C_r + iC_1\delta_m - \kappa_T - \left[\kappa_n + \kappa_T \left(x - \frac{3}{2} \right) \right] I_i, \quad (\text{C1})$$

where

$$I_i = \frac{2}{\sqrt{\pi}} \int \frac{\sqrt{E} e^{-E}}{E - x} dE. \quad (\text{C2})$$

Since we are interested in linearly unstable solutions, x has a positive imaginary part, and we can express I_i as

$$\frac{I_i}{2} = 1 - e^{-x} \sqrt{-\pi x} - 2\sqrt{x} W(\sqrt{x}), \quad (\text{C3})$$

where W is the Dawson integral^{32,33}

$$W(z) = \frac{1}{2} \sqrt{\pi} e^{-z^2} \text{erfi}(z). \quad (\text{C4})$$

Since the marginal solution in the $\delta = 0$ limit is $\omega = 3m\omega_d/2$,⁵ we substitute x by $\delta\omega = (x - 3/2)m\omega_d$. The dispersion relation is then developed to the second order in $\delta\omega$. This yields

$$\begin{aligned} D[x] = & C_r + iC_1\delta_m - \kappa_T - (2 + \alpha)\kappa_n \\ & - \left[(2 + \alpha)\kappa_T - \left(2 + \frac{2}{3}\alpha \right) \kappa_n \right] \frac{\delta\omega}{m} \\ & + \left[\left(2 + \frac{2}{3}\alpha \right) \kappa_T - \left(\frac{2}{3} + \frac{1}{9}\alpha \right) \kappa_n \right] \frac{\delta\omega^2}{m^2} \\ & + O[\delta\omega^3], \end{aligned} \quad (\text{C5})$$

where $\alpha = [1 - \text{erfi}(\sqrt{3/2})] \sqrt{6\pi} e^{-3/2}$.

Solving $D[x] = 0$ for $\delta\omega$ yields two solutions. The root that is consistent with our assumptions is

$$\frac{\delta\omega}{m} = \frac{3(2 + \alpha)\kappa_T - 2(3 + \alpha)\kappa_n + \sqrt{\Delta}}{4(3 + \alpha)\kappa_T - (4 + 2\alpha/3)\kappa_n}, \quad (\text{C6})$$

where

$$\begin{aligned} \Delta = & [3(2 + \alpha)\kappa_T - 2(3 + \alpha)\kappa_n]^2 \\ & - 4[6(3 + \alpha)\kappa_T - (6 + \alpha)\kappa_n] \\ & [C_r + iC_1\delta_m - \kappa_T - (2 + \alpha)\kappa_n]. \end{aligned} \quad (\text{C7})$$

The real frequency and growth rate are then obtained as $\omega = 3m\omega_d/2 + \text{Re}(\delta\omega)$ and $\gamma = \text{Im}(\delta\omega)$. They are shown in Fig. 5 (labeled ‘‘Analytic, $J_0 = 1$ ’’).

We now consider a more accurate approximation of J_0 ⁶

$$J_0(E) \approx \left(1 - \frac{m^2 \rho_0^2}{4} E \right) \left(1 - \frac{k^2 \delta_b^2}{4} E \right), \quad (\text{C8})$$

where we have taken $q_0/a = 1$ to lighten the equations. This factor can be recovered by the substitution $\rho_0 \rightarrow q_0\rho_0/a$. We take $\kappa_n = 0$ for the sake of clarity and concision. We obtain the dispersion relation

$$\begin{aligned} D[x] = & C_r + iC_1\delta_m - \eta_{mk}\kappa_T - (2 + \alpha)\eta_m\eta_k\kappa_T \frac{\delta\omega}{m} \\ & + \left[\left(2 + \frac{2}{3}\alpha \right) \eta_m\eta_k\beta \left(1 + \frac{\alpha}{2} \right) \right] \kappa_T \frac{\delta\omega^2}{m^2} + O[\delta\omega^3]. \end{aligned} \quad (\text{C9})$$

Here, we have defined

$$\eta_m = 1 - \frac{3}{4}(m\rho_0)^2 + \frac{9}{64}(m\rho_0)^4, \quad (\text{C10})$$

$$\eta_k = 1 - \frac{3}{4}(k\delta_b)^2 + \frac{9}{64}(k\delta_b)^4, \quad (\text{C11})$$

$$\beta = \left[(m\rho_0)^2 - \frac{3}{8}(m\rho_0)^4 \right] \eta_k + \left[(k\delta_b)^2 - \frac{3}{8}(k\delta_b)^4 \right] \eta_m, \quad (\text{C12})$$

and

$$\begin{aligned} \eta_{mk} = & \left[1 - \frac{3}{4}(m\rho_0)^2 + \frac{15}{64}(m\rho_0)^4 \right] \\ & - 3(k\delta_b)^2 \left[\frac{1}{4} - \frac{5}{16}(m\rho_0)^2 + \frac{35}{256}(m\rho_0)^4 \right] \\ & + 15(k\delta_b)^4 \left[\frac{1}{64} - \frac{7}{256}(m\rho_0)^2 + \frac{63}{4096}(m\rho_0)^4 \right]. \end{aligned} \quad (\text{C13})$$

The root that is consistent with our assumptions is

$$\frac{\delta\omega}{m} = \frac{3\eta_m\eta_k(2+\alpha)\kappa_T + \sqrt{\Delta}}{\left[(4\eta_m\eta_k(3+\alpha) + 3\beta(2+\alpha))\kappa_T \right]}, \quad (\text{C14})$$

where

$$\begin{aligned} \Delta = & [3(2+\alpha)\eta_k\eta_m\kappa_T]^2 \\ & - 4[18\beta(2+\alpha) + 6\eta_k\eta_m(3+\alpha)\kappa_T] \\ & [C_r + iC_1\delta_m - \eta_{mk}\kappa_T]. \end{aligned} \quad (\text{C15})$$

Applications are shown in Fig. 5 (labeled ‘‘Analytic’’) and Fig. 6.

It can be easily checked that substituting $\kappa_n = 0$ into Eq. (C6) yields the same expression as substituting $\eta_m = \eta_k = \eta_{mk} = 1$ and $\beta = 0$ (the $J_0 = 1$ limit) into Eq. (C14).

The advantage of such analytic expressions, compared to solving the dispersion relation numerically, is that it significantly speeds up the exploration of the space of input parameters.

¹X. Garbet, Y. Idomura, L. Villard, and T. Watanabe, *Nucl. Fusion* **50**, 043002 (2010).

²T.-H. Watanabe and H. Sugama, *Nucl. Fusion* **46**, 24 (2006).

³H. Biglari, P. H. Diamond, and P. W. Terry, *Phys. Fluids* **31**, 2644 (1988).

⁴M. Tagger, G. Laval, and R. Pellat, *Nucl. Fusion* **17**, 109 (1977).

⁵G. Depret, X. Garbet, P. Bertrand, and A. Ghizzo, *Plasma Phys. Controlled Fusion* **42**, 949 (2000).

⁶Y. Sarazin, V. Grandgirard, E. Fleurence, X. Garbet, P. Ghendrih, P. Bertrand, and G. Depret, *Plasma Phys. Controlled Fusion* **47**, 1817 (2005).

⁷G. Darmet, P. Ghendrih, Y. Sarazin, X. Garbet, and V. Grandgirard, *Vlasovia 2006: The Second International Workshop on the Theory and Applications of the Vlasov Equation* [Commun. Nonlinear Sci. Numer. Simul. **13**, 53 (2008)].

⁸T. Cartier-Michaud, P. Ghendrih, V. Grandgirard, and G. Latu, *ESAIM: Proc.* **43**, 274 (2013).

⁹T. Cartier-Michaud, P. Ghendrih, Y. Sarazin, G. Dif-Pradalier, T. Drouot, D. Estve, X. Garbet, V. Grandgirard, G. Latu, C. Norscini, and C. Passeron, *J. Phys.: Conf. Ser.* **561**, 012003 (2014).

¹⁰B. Kadomtsev and O. Pogutse, *Nucl. Fusion* **11**, 67 (1971).

¹¹W. Manheimer, *Introduction to Trapped-Particle Instability in Tokamaks. ERDA Critical Review Series* (Technical Information Center, Energy Research and Development Administration, University of Michigan, Ann Arbor, 1977).

¹²W. M. Tang, G. Rewoldt, and L. Chen, *Phys. Fluids* **29**, 3715 (1986).

¹³A. Jarmén, *Phys. Scr.* **40**, 658 (1989).

¹⁴J. A. Crottinger and T. H. Dupree, *Phys. Fluids B* **4**, 2854 (1992).

¹⁵H. L. Berk, B. N. Breizman, and M. Pekker, *Phys. Plasmas* **2**, 3007 (1995).

¹⁶T. Drouot, E. Gravier, T. Reveille, A. Ghizzo, P. Bertrand, X. Garbet, Y. Sarazin, and T. Cartier-Michaud, *Eur. Phys. J. D* **68**, 280 (2014).

¹⁷T. Drouot, E. Gravier, T. Reveille, M. Sarrat, M. Collard, P. Bertrand, T. Cartier-Michaud, P. Ghendrih, Y. Sarazin, and X. Garbet, *Phys. Plasmas* **22**, 082302 (2015).

¹⁸P. H. Diamond and H. Biglari, *Phys. Rev. Lett.* **65**, 2865 (1990).

¹⁹O. T. Kingsbury and R. E. Waltz, *Phys. Plasmas* **1**, 2319 (1994).

²⁰T. H. Dupree, *Phys. Fluids* **15**, 334 (1972).

²¹I. Bernstein, J. Greene, and M. D. Kruskal, *Phys. Rev.* **108**, 546 (1957).

²²P. W. Terry, P. H. Diamond, and T. S. Hahm, *Phys. Fluids B* **2**, 2048 (1990).

²³P. H. Diamond, P. L. Similon, P. W. Terry, C. W. Horton, S. M. Mahajan, J. D. Meiss, M. N. Rosenbluth, K. Swartz, T. Tajima, R. D. Hazeltine, and D. W. Ross, *Plasma Phys. Controlled Fusion Res. IAEA-CN-41/D-1-2*, 259 (1983).

²⁴P. Diamond, S.-I. Itoh, and K. Itoh, *Modern Plasma Physics: Volume 1, Physical Kinetics of Turbulent Plasmas*, Modern Plasma Physics (Cambridge University Press, Cambridge, 2010).

²⁵Y. Kosuga, S. I. Itoh, P. H. Diamond, K. Itoh, and M. Lesur, *Phys. Plasmas* **21**, 102303 (2014).

²⁶Y. Kosuga, S. I. Itoh, P. H. Diamond, K. Itoh, and M. Lesur, *Plasma Fusion Res.* **9**, 3403018 (2014).

²⁷Y. Kosuga, S.-I. Itoh, P. H. Diamond, K. Itoh, and M. Lesur, ‘‘Role of phase space structures in collisionless drift wave turbulence and impact on transport modeling,’’ *Nuclear Fusion* (to be published).

²⁸Y. Kosuga, S.-I. Itoh, P. H. Diamond, and K. Itoh, *Plasma Phys. Controlled Fusion* **55**, 125001 (2013).

²⁹E. Gravier, M. Lesur, T. Reveille, and T. Drouot, *Phys. Plasmas* **23**, 092507 (2016).

³⁰T. Cartier-Michaud, ‘‘Vérification de codes et réduction de modèles: Application au transport dans les plasmas turbulents,’’ PhD thesis (Aix-Marseille Université, 2015).

³¹F. Palermo, X. Garbet, A. Ghizzo, T. Cartier-Michaud, P. Ghendrih, V. Grandgirard, and Y. Sarazin, *Phys. Plasmas* **22**, 042304 (2015).

³²H. G. Dawson, *Proc. London Math. Soc.* **s1-29**, 519 (1897).

³³M. Abramowitz and I. A. Stegun, *Appl. Math. Ser.* **55**, 62 (1966).